Title: *In situ* observations of cracking in constrained sintering

Authors: Joseph R. Carazzone, Michael D. Bonar, Henry W. Baring, Mark A. Cantu, Zachary C. Cordero

Affiliation: Materials Science and NanoEngineering, Rice University, Houston, TX 77005

Abstract: In this paper we examine the long-standing problem of cracking during constrained sintering of a powder aggregate. Using binder jet 3D printing, we prepare ceramic green bodies in the form of center-notched panels, then use *in situ* imaging to observe how cracks nucleate and grow from the notch as the material sinters under restraint. Quantitative image analysis allows us to identify important characteristics of the sinter-cracking process, indicating a framework for analyzing the problem and developing methods for avoiding it, including representation of sinter-cracking as a creep crack growth process, use of fracture mechanics parameters to design specimen geometries that do not exceed critical stress intensities, and the possibility of exploiting the inherently ductile nature of sinter-cracking to mitigate damage.

Keywords: sinter/sintering, fracture, solid freeform fabrication, in situ imaging

Corresponding Author: zc29@rice.edu; 713-348-2904

1. Introduction

Sintering is a high-temperature process used to transform loosely bound powder aggregates into near net-shaped objects with controlled amounts of porosity. When a powder aggregate is sintered, its structure evolves to lower its excess surface energy. Necks grow between adjacent particles to reduce the local curvature at their contacts, and the entire aggregate densifies to eliminate surface area (1). In many sintering applications, external restraints can prevent a

powder aggregate from densifying in one or more directions. Friction, for example, can prevent a thin film sintering on a rigid substrate from shrinking in the in-plane directions (2,3). Under these constrained sintering conditions, internal stresses can develop in the sintering material, and in extreme cases, these stresses can grow so large that they tear the aggregate apart (4). This fracture process, here referred to as sinter-cracking, degrades product quality, lowers yield, and proves highly undesirable.

Previous investigations have approached the problem of sinter-cracking with theoretical (3,5), experimental (4,6), and computational methods (7,8). In a detailed mechanical analysis of a sintering thin film containing a crack-like flaw and constrained by a planar rigid substrate, Jagota and Hui (3) found that growth of the flaw in the early stage of sintering can be predicted using the stress intensity factor. Their theoretical findings were later confirmed experimentally by Bordia and Jagota (4) through testing a range of flaw sizes in both glass and alumina films. However, their observations were limited because they were not able to monitor the fracture process directly, thus sacrificing details about the manner of cracking onset, shape change at high temperatures, and the rate of crack growth.

One way of solving the problem of direct monitoring of sinter-cracking has been demonstrated by Martin and coworkers, who used the discrete element method (DEM) to simulate crack propagation in sintering crystalline materials (8). These investigators found microstructural evolution and crack propagation behaviors which strongly depended on the amount of particle rearrangement allowed by the tangential contact viscosity between the particles. Importantly, the DEM simulations allowed these investigators to measure the crack growth rate and the forces acting on the particles, allowing direct observation of the sintering stress. However, the accuracy of their results, and of DEM more generally, depends on the accuracy of the theoretical model

used to define the contact forces, and typically the constitutive laws used in DEM are valid for only certain stages of sintering. Other limitations of DEM include computational difficulty associated with treating large systems of particles.

In this work, we address these challenges with studying sinter-cracking using 3D printing and high-temperature imaging. Following the method of fracture mechanics in the understanding of cracking in materials, we use binder jet 3D printing to prepare notched tensile test specimens with precisely controlled geometries and known stress concentration factors. We then study the sinter-cracking behavior of these specimens using high-temperature imaging experiments, in which a center-notched specimen is sintered while being restrained in a metal frame. The sintering material experiences a state of self-induced stress, and high temperature radiation facilitates direct observation of cracking behavior with high resolution digital photography. From the images we can measure quantities relevant to the sinter-cracking process, such as relative density and crack size as functions of time.

2. Experimental procedure

Center-notched rectangular panel specimens were fabricated on an ExOne Innovent binder jet 3D printer according to the design shown in Fig. 1. In the binder jetting process, objects are built layer-by-layer by joining powder feedstock with an organic binder (9). First, a layer of powder material is dispensed from a hopper onto the build surface, then smoothed by a rotating drum known as the recoater. Then binder, here an aqueous solution of polyethylene glycol precursors[*], is dispensed by a printhead onto the regions of powder that will form the printed objects. An infrared heating lamp partially cures the binder, then the build platform lowers by a distance

[*] 7100037CL, ExOne, North Huntingdon, PA.

equal to the layer thickness and the process is repeated. The powder material used for this work was commercial cupric oxide of -200 mesh particle size and a composition by weight of 91.0% CuO, 3.0% Cu_2O, and 5.5% talc[†]. CuO was chosen for its low melting point, allowing densification to be observed on a feasible time scale at temperatures available to the experimental setup. Scanning electron microscopy (SEM) revealed the microstructure of the powder to comprise irregular polycrystalline aggregates, as shown in Fig. 2. Image analysis determined the particle size distribution to be bimodal with average values of 1 and 9 μm. This μm-scale particle size was amenable to the powder spreading step of the binder jetting process. Specimens were printed with a layer thickness of 80 μm; the direction of the build was normal to the major specimen face shown in Fig. 1a.

The fracture specimens had a thin rectangular gauge section to promote a planar stress state and thicker grip sections to prevent cracking at the points of restraint. The center notch was located in the middle of the gauge section. The dimensions of the elliptical notch (major axis = 3.8 mm; minor axis = 0.7 mm) and the panel (width = 9.1 mm) lead to a calculated stress concentration factor of 14[‡]. The specimens were restrained in a stainless steel frame using stainless steel pins as shown in Fig. 1. The result is a uniaxially restrained system which promotes a uniaxial stress state that will act on the central notch, as in a traditional fracture mechanics test. The openings cut through both faces of the frame allow the specimen to be viewed at radiating temperatures with sufficient contrast for measuring its dimensions; the open slot in the top of the frame accommodates the restraining pin while allowing the specimen to expand freely in the vertical direction, thereby avoiding thermal expansion mismatch stresses. Effects due to gravity for this

[†] CU-601, Atlantic Equipment Engineers, Upper Saddle River, NJ. The Cu_2O and talc included by the supplier represent minor components.
[‡] K_{tg} for an elliptical hole in a finite-width thin element, p. 335 of Ref. (11).

setup are expected to be negligible: the stress due to gravity for the specimen geometry is calculated to be ~ 0.5 kPa[§], orders of magnitude less than sintering pressures reported for other oxide materials (6,10). To control for the effect of the notch on cracking behavior, a specimen without a notch was also tested.

Sinter-cracking experiments were carried out in a tube furnace held at 1000 °C (80% of the melting temperature (T_{melt}) of CuO) with a maximum heating rate of 10 °C/min. By leaving one end of the tube open, *in situ* monitoring of the specimen was performed using a 22.3 megapixel Canon SLR camera equipped with a 200 mm lens and 2x extender. Photographs were taken at 5 second intervals. A K-type thermocouple placed behind the specimen allowed direct monitoring of its temperature during the experiment. Image analysis was performed with Fiji (12) using binary thresholding with particle and point analysis to determine relative density and crack length as functions of time. Quantitative results are presented here for a single specimen; however, the data are characteristically consistent with multiple experiments of this type.

A specimen cross section was obtained by impregnating the specimen with transparent epoxy, followed by polishing with SiC and 6 μm diamond paste. A second epoxy infiltration of the porous specimen surface was performed with subsequent polishing to 1 μm diamond paste, followed by 30 min of vibratory polish with colloidal silica. The polished surface was sputter coated with 1 nm of gold prior to imaging under high vacuum SEM. Image stitching was performed using commercial software[**].

3. Results and discussion

[§] Stress due to gravity was calculated as DgH, where D is the density of the green body, g is the acceleration due to gravity, and H is the height of the gauge section of the specimen.
[**] Adobe Photoshop CC 2018, Adobe Systems Inc., San Jose, CA

3.1. Qualitative observations

Fig. 3 is a series of photographs showing the specimen at various stages of sintering. At temperatures below 1000 °C, shape change in the specimen is minimal with only slight vertical opening of the notch, and the specimen profile shown in Fig. 3a is approximately identical to that at room temperature. As the specimen reaches the sintering temperature, opening of the notch is accelerated while the initially sharp notch roots become rounded. The straight specimen edges adjacent to the notch taper inward, indicating the concentrated stress field around the roots of the notch. After 114 minutes at 1000 °C, the height of the notch has increased to 1.0 mm, its roots have become less sharp, and a small triangular crack has initiated at its right side, as shown in Fig. 3b. As densification continues, the crack grows in both its length and opening distance, the included angle of the crack increases to 65° (corresponding to a crack blunting mechanism), and a new crack initiates on the opposite side surface of the ligament at approximately the same vertical position (Fig. 3c). Also visible in this image is a bright region ahead of the original crack representing a difference in emissivity of the material, probably caused by a process zone of accumulated damage ahead of the crack tip. Finally, just before fracture, Fig. 3d shows a jagged crack surface, a large dangling ligament, and a thin connective particle strand bridging the crack void, all pointing to a tortuous crack path and a highly ductile fracture mode.

The observed increase of the included angle of the crack is caused by continued densification of material adjacent to the crack and reveals the ductile nature of sinter-cracking. The sinter-cracking process displayed in these images is characterized by a slow-tearing fracture mode with periods of growth interrupted by periods of crack arrest. This ductile character is made particularly evident by compiling the still images into a movie, which is available as supplemental material Fig. S1.

The nature of the crack and the evolution of damage in the sintering material can be better understood through close examination using SEM. In Fig. 4, a series of micrographs from interrupted sintering experiments is shown, demonstrating the progression from green body to fractured material. The appearance of the as-printed specimen in Fig. 4a is of uniform roughness and the presence of the binder is evident by a greater brightness than in Figs. 4b and 4c. Sites of likely crack nucleation are already evident as areas of greater roughness around the notch, where the printing process failed to form continuous layer regions. In Fig. 4b, the binder has been removed by raising the specimen to 1000 °C and allowing it to cool immediately. Already, the nucleation of a crack can be seen, as the rough region at the notch root has become more porous due to slight densification and vertical opening of the notch. Other defects have become visible in the form of vertically aligned pockets and furrows, artifacts of the binder jetting process that are likely due to dispensing of the binder: this process involves forceful application of the liquid to the powder, and that along with the binder's surface tension can lead to disruption of the initially smooth powder surface. After 30 min of sintering at 1000 °C, the porous material at the notch root has developed into an open crack, propagating through printing defects in a direction mostly perpendicular to the direction of restraint; the printing defects observed at earlier stages have been exacerbated by the sintering cycle. The influence of the stress field ahead of the crack can be seen by tapering of the furrows toward the crack, and a process zone of damage is evidenced by the development of porous regions and growth of voids ahead of the continuous crack. The triangular crack shape that was evident in the photographs can also be observed here, reminiscent of the fracture geometry observed by several other investigators in studies on sinter-cracking in notched powder rings (13), rigid inclusions (6), and pre-cracked films (4).

In their detailed investigation of sinter-cracking films, Bordia and Jagota observed a tortuous crack path in alumina densifying under planar restraining conditions. They found diffuse damage zones ahead of the main crack as well as a rough fracture surface and bridging ligaments within the crack, similar to features observed here (4). For example, magnification of the boxed region in Fig. 4c gives a descriptive view of the particle-scale activity that has resulted from the cracking process as shown in Fig. 5. Immediately obvious are ruptured strands of particles decorating the surface of the crack: these features indicate a slow tearing, ductile fracture mode whereby sintering material is gradually pulled apart, leading to elongation of connected material just prior to rupture.

The findings here can be related to previous work, and thus related to an analytical framework that aids increased understanding of sinter-cracking. The dangling particle ligaments shown in Fig. 5 are similar in appearance to the elongated strands observed on the alumina fracture surface by Bordia and Jagota, pointing to a similar fracture mode. The microstructure of these strands, an array of connected material thinned down to a terminus of just a few particles, is reminiscent of the desintering phenomenon observed by Sudre and Lange in a zirconia system, where the mechanism of final rupture was attributed to tensile forces and grain coarsening (5). Also important to note is the still-connected material spanning the crack opening in the background of Fig. 5. Such crack-bridging ligaments will toughen a material against fracture, lowering the stress intensity at the crack tip, and have been analyzed in the context of high-temperature creep cracking in oxide systems (14).

While details such as shape change and particle behavior can be gleaned from surface imaging of the specimen, a polished cross section of the material allows analysis of the relative density and its variation with position around the notch and the crack. Such measurements can lead to an

understanding of the stress field and how it may be quantified, as well as its influence on microstructural evolution. Fig. 6 shows a cross section approximately halfway through the thickness of the specimen shown in Figs. 4c and 5. Easily seen in the cross section are the defects arising from the binder jetting process (vertical furrows and aligned pockets). The width of the furrows and diameter of the pockets are on the order of a typical binder droplet (50 μm), and their vertical alignment is consistent with the travel of the binder jets during the printing process (perpendicular to the recoater travel direction as indicated in the figure). While the impact of the binder and the effect of its surface tension on the arrangement of particles in the powder bed is the most likely cause of the observed defects, another possible source is uneven spreading of the material, a problem for fine powders in particular. The ultimate result of these defects is to lower the effective toughness of the sintering powder aggregate, as would defects formed through other powder processing methods (15). These defects influence the trajectory of the crack during sintering just as defects in fully dense ceramics affect their toughness and fracture behavior.

In addition to printing defects, trends can be seen in the porosity of the sintered material in different regions of the specimen. Directly above and below the notch, the material has densified uniformly, and the regions show lower overall porosity. This is consistent with the lower tensile stresses near the horizontal free surfaces.

Moving away from the notch, interesting trends can be observed in the sintered material. The crack emanates from the side of the notch with a large opening devoid of material, but at farther points along its length, bridging particle strands can be seen. These strands are porous, an indication of the gradual tearing involved in the fracture mode. What appeared on the surface of the specimen to be a single main crack is found here to have divided into separate branches, with highly porous material lying between them. The implication is that the sinter-cracking process is

ductile, and the rupture of material in one region of the specimen does not immediately propagate to adjacent material, thus providing a toughness that is able to resist catastrophic failure.

Above the tip of the main crack, the material is more porous. Unlike the material lying above the notch, the material in this region experienced the full effect of restraint at the onset of densification. As the crack opens, the restraint on the adjacent material is relaxed; the specimen becomes more compliant, and densification is allowed to progress. Ahead of the crack, however, the stress due to restrained densification remains concentrated. As can be observed in the cross section, dilation of printing defects and separation of bound material reveal a process zone of damage, a response to the intensification of stress in the material ahead of the crack tip prior to its linking with the main crack. Beyond this process zone is a region of lower porosity where the material was free to densify due to lateral shrinkage of the material, possibly aided by particle rearrangement. Above the process zone the material can also be seen to have a lower porosity.

3.2. Quantitative image analysis

The major advantage of *in situ* imaging is the ability to monitor changes in the sintering specimen over time, allowing correlation between quantities such as crack growth, densification, and their respective rates, quantities difficult to obtain through interrupted experiments. Using image analysis software (12), photographs such as those shown in Fig. 3 can be thresholded, converted into binary images, and used to evaluate relative density and crack growth in the sintering specimen as functions of time.

3.2.1. Densification

Measurement of densification from the *in situ* images was based on the change in projected area of the sintering specimen. The measurement assumes a uniform density throughout the specimen. The specimen cross section shown in Fig. 6 indicates that this is not the case and that the local density varies with position around the notch. This is borne out by image analysis of the cross section, which reveals that the average relative density far from the notch is greater than that near the notch. Nonetheless, the measurement provides insight into the instantaneous densification behavior of the material at sintering temperatures, a quantity otherwise difficult to obtain. This measurement also assumes a negligible overall vertical shrinkage due to the restraint placed on the specimen as well as isotropic horizontal shrinkage in the two lateral dimensions due to random particle packing; it does not assume uniform specimen thickness, which is appropriate to account for the effect of the notch. Based on the given assumptions and the definition of density, the following equation is derived to compute the instantaneous average relative density of the specimen, ρ:

$$\rho = \rho_0 \frac{A_0 W_0}{A\ W}, \tag{1}$$

where ρ_0 is the initial average relative density of the specimen, A and A_0 are the instantaneous and the initial projected area of the specimen, and W and W_0 are the instantaneous and the initial projected width of the specimen. ρ_0 was determined from the mass and volume of a printed cylindrical specimen after it was heated past binder burnout such that sintering with minimal densification occurred. We approximate W_0 as A_0/H and W as A/H, where H is the projected height of the specimen between the grips (taken to be constant). This accounts for the variation in the width of the specimen along its height due to the effect of the notch.

The resulting plot of density versus time is shown with the corresponding temperature profile in Fig. 7, beginning at a temperature of 845 °C. Data are shown until the point of complete fracture of the right side of the specimen. At temperatures below 900 °C, densification does not occur; shrinkage due to binder burnout is negligible due to its low volume fraction and the specimen remains at its initial relative density of 0.33. After passing 900 °C, the rate of densification increases rapidly from zero to a maximum of 0.042 hr^{-1} until the isothermal stage is reached, after which the rate begins to monotonically decrease to a final value of 0.005 hr^{-1}, yielding a final average density of 0.48.

Determination of specimen density through the *in situ* images can be compared with image analysis of a polished cross section of the specimen microstructure like that shown in Fig. 6. From the *in situ* images, the average density of the specimen shown in Fig. 4c was found to be 0.39. The average relative density of the microstructure based on image analysis of the cross section is 0.44, in good agreement with the value determined from the *in situ* images.

During densification, stress builds in the specimen due to the vertical restraint placed on it. This stress acts on the notch and causes initiation and growth of cracks. It can be seen from the plot that, although cracking begins at 1.4 hours, densification continues at a nearly steady rate, thus continuing to drive the fracture process. The continuously diminishing rate of densification is consistent with previous observations of constrained sintering in multilayer composite films (16). For the case of the un-notched specimen, the densification curve is similar in shape, although the initial stage is more rapid. This may be caused by a more uniform stress distribution in the material due to the lack of a notch.

3.2.2. Crack growth

Crack length is plotted against time in Fig. 8, spanning the same period of time as that for densification; the plot terminates at the moment of complete fracture of the right side of the specimen. Length of the crack was calculated from the *in situ* images as the horizontal distance of the crack tip from the notch root, taking into account the change in position of the notch root due to densification. This process was carried out manually using the point analysis feature of Fiji. Position of the original notch root was tracked by visual interpretation of the change in shape of the notch; position of the crack tip was regarded as the rightmost edge of the continuous background emanating from the notch as the crack grew.

Cracking begins around the same time as densification, highlighting the correlation between the two processes. The graph reveals interesting characteristics of the sinter-cracking process: regions of steady growth are separated by crack-arrest phases in which the crack length actually decreases due to continued densification of the material; the regions of growth exhibit roughly the same rate of crack length increase over time (an average of 0.29 mm/hour); the regions of arrest and shrinkage are likewise similar (average rate of -0.03 mm/hour); and the final stage prior to total failure is marked by a slower increase in crack length which we attribute to the overall change in shape of the specimen rather than the rupture of new material. That the cracking behavior observed here is caused by the notch is made clear by comparison with the un-notched control experiment: no major fracture was observed in the tensile specimen prepared without a notch. This demonstrates the tendency of the forces in a sintering material to balance, leading to densification. It is possible, as observed by Martin *et al.*, for cracking to occur without the presence of a notch: when the tangential viscosity acting between particles is sufficiently large, particle rearrangement is inhibited and a buildup of internal stress occurs, leading to

rupture of particle contacts (8). In the present case, however, the force-amplifying effect of a stress-concentrating defect (the notch) was required to disrupt densification and cause cracking.

A graph of the type shown in Fig. 8 makes it possible to relate sinter-cracking behavior to the traditional fracture mechanics framework: sinter-cracking is closely related to creep cracking, where low stresses and high temperatures lead to gradual, time-dependent failure (17). One essential quantity in this framework is the rate of crack growth with respect to time (18), a quantity made easily obtainable by *in situ* monitoring. Such measurements, if combined with knowledge of the sintering stress, can lead to determination of important fracture mechanics parameters like the stress intensity factor; this in turn can lead to experimental evaluation of the sintering material's fracture toughness.

The final plot in Fig. 9 combines the outcome of both density and crack length measurements. Immediately evident at low relative densities is a brief incubation period in which densification takes place without any cracking. A certain amount of microstructural change and stress buildup is required before crack initiation takes place. The regions of growth and arrest seen in Fig. 8 become more pronounced in Fig. 9, and it is clear that a crack arrest mechanism is in effect. While densification during crack growth is to be expected, the arrest and decrease of crack length while densification continues is surprising. This indicates the existence of microstructural processes which cause the crack to stop growing, and may be caused by phenomena such as particle rearrangement (7,8) and stress relaxation (16,19) identified by others as important to inhibiting sinter-crack development. The jumps in crack length that lie between the arrest phases may arise from the main crack linking with voids lying ahead of it in the process zone, such as the printing defects observed in Fig. 6. Such process zone influence, also observed in sintering

films (4) as well as fully dense materials (17), may be a function of variable structure in the material and will have a strong effect on sinter-cracking behavior.

4. Conclusion

We have presented a novel method for *in situ* observation of cracking caused by the self-stress induced in materials sintering under restraint. The method enables direct observation of the time-dependent fracture process and allows measurement of quantities such as density and crack length as functions of time. Our method is enabled by recent advances in 3D printing technology which make possible the preparation of test specimens that are difficult to produce through traditional powder processing methods. Through analysis of both *in situ* and *ex situ* data, we identify several important phenomena:

- The fracture mode is ductile in nature, with a tortuous crack path, significant crack-bridging ligaments, and evidence of slow tearing through particle strand rupture;
- During the growth phase, the rate of crack length increase is roughly linear and constant across separate crack growth phases;
- Growth phases are separated by distinct phases of arrest in which the crack length decreases due to continued densification.

Finally, we observe that *in situ* monitoring experiments like that presented here enable an advance in the understanding of sinter-cracking by making available important fracture mechanics quantities such as the crack growth rate. When combined with knowledge of the sintering stress, these measurements can lead to the evaluation of the fracture toughness of a sintering material and thus design of processing regimens that preclude cracking during sintering.

Acknowledgements

We gratefully acknowledge Joshua J. Wagner of Rice University for insightful discussion of the binder jetting process. We also thank Dr. Amy Elliott of the Oak Ridge National Laboratory for financial support of this work.

References

1. Swinkels FB, Ashby MF. A second report on sintering diagrams. Acta Metall. 1981;29(2):259–281.

2. Jagota A, Hui CY. Mechanics of sintering thin films — I. Formulation and analytical results. Mech Mater. 1990 Sep 1;9(2):107–19.

3. Jagota A, Hui CY. Mechanics of sintering thin films — II. Cracking due to self-stress. Mech Mater. 1991 May 1;11(3):221–34.

4. Bordia RK, Jagota A. Crack growth and damage in constrained sintering films. J Am Ceram Soc. 1993;76(10):2475–2485.

5. Sudre O, Lange FF. The effect of inclusions on densification; III, the desintering phenomenon. J Am Ceram Soc. 1992;75(12):3241–3251.

6. Ostertag CP, Charalambides PG, Evans AG. Observations and analysis of sintering damage. Acta Metall. 1989 Jul 1;37(7):2077–84.

7. Henrich B, Wonisch A, Kraft T, Moseler M, Riedel H. Simulations of the influence of rearrangement during sintering. Acta Mater. 2007 Jan;55(2):753–62.

8. Martin CL, Camacho-Montes H, Olmos L, Bouvard D, Bordia RK. Evolution of Defects During Sintering: Discrete Element Simulations. J Am Ceram Soc. 2009 Jul 1;92(7):1435–41.

9. Nandwana P, Elliott AM, Siddel D, Merriman A, Peter WH, Babu SS. Powder bed binder jet 3D printing of Inconel 718: Densification, microstructural evolution and challenges. Current Opinion in Solid State and Materials Science. 2017 Aug 1;21(4):207–18.

10. Cheng T, Raj R. Measurement of the Sintering Pressure in Ceramic Films. Journal of the American Ceramic Society. 1988 Apr 1;71(4):276–80.

11. Pilkey WD, Pilkey DF, Peterson RE. Peterson's stress concentration factors. Third edition. 2008. 522 p.

12. Schindelin J, Arganda-Carreras I, Frise E, Kaynig V, Longair M, Pietzsch T, et al. Fiji: an open-source platform for biological-image analysis. Nat Methods. 2012 Jul;9(7):676–82.

13. Lange FF. Densification of powder rings constrained by dense cylindrical cores. Acta Metall. 1989 Feb 1;37(2):697–704.

14. Evans AG, Dalgleish BJ. Some Aspects of the High Temperature Performance of Ceramics and Ceramic Composites. Ceram Eng Sci Proc. 1986;7:1073.

15. Lange FF, Metcalf M. Processing-Related Fracture Origins: II, Agglomerate Motion and Cracklike Internal Surfaces Caused by Differential Sintering. J Am Ceram Soc. 1983 Jun 1;66(6):398–406.

16. Cheng T, Raj R. Flaw Generation During Constrained Sintering of Metal-Ceramic and Metal–Glass Multilayer Films. Journal of the American Ceramic Society. 1989 Sep 1;72(9):1649–55.

17. Riedel H. Creep Crack Growth. In: Wei RP, Gangloff RP, editors. ASTM STP 1020. Philadelphia: American Society for Testing and Materials; 1989. p. 101–26.

18. Turner CE, Webster GA. Application of fracture mechanics to creep crack growth. Int J Fract. 1974 Sep 1;10(3):455–8.

19. Bordia RK, Raj R. Sintering Behavior of Ceramic Films Constrained by a Rigid Substrate. J Am Ceram Soc. 1985 Jun 1;68(6):287–92.

Figures and captions

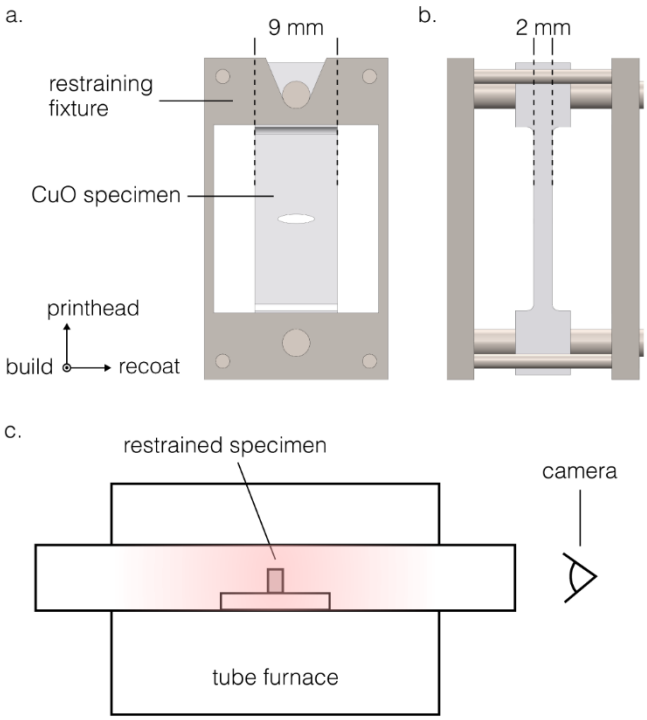

Fig. 1. (a) Front profile of the notched panel specimen placed in the stainless steel restraining fixture, showing relevant dimensions. The open slot in the top part of the fixture prevents stress build-up due to thermal expansion. The axes indicate the direction of build, printhead travel, and powder recoat. (b) Side profile of the specimen and fixture. (c) Experimental setup used to monitor sinter-cracking *in situ*.

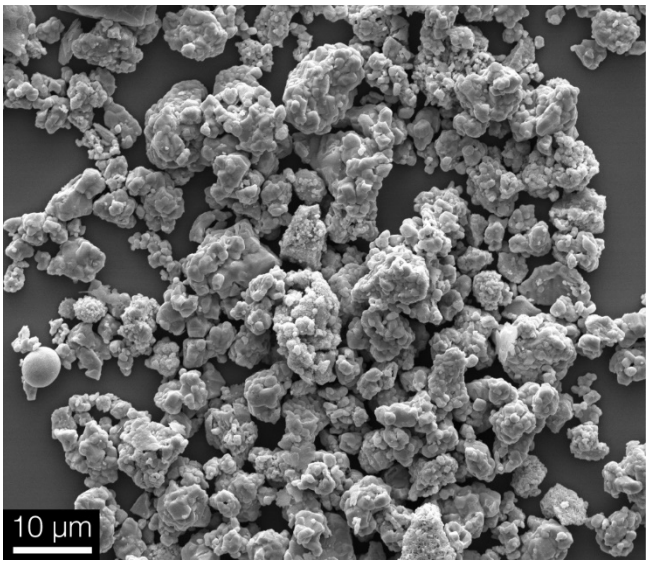

Fig. 2. SEM micrograph of powder feedstock showing its irregular morphology. The particle size distribution was bimodal with average values of 1 and 9 µm.

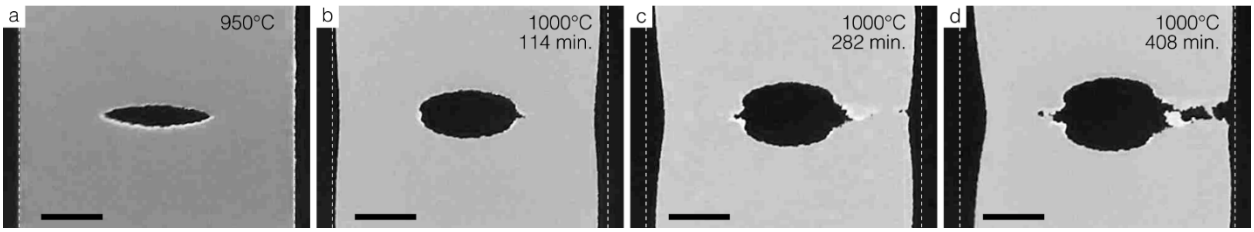

Fig. 3. Photographs showing changes in the specimen over the course of sintering: (a) the shape of the specimen before significant change begins; (b) after widening of the notch and initiation of a crack; (c) the crack has grown 0.22 mm from the notch root and a brightly colored process zone is visible at its tip; (d) near complete fracture of the original 2.6 mm ligament with a thin particle strand bridging the void. Times are referenced to when the maximum sintering temperature was reached. Scale bars are 2 mm.

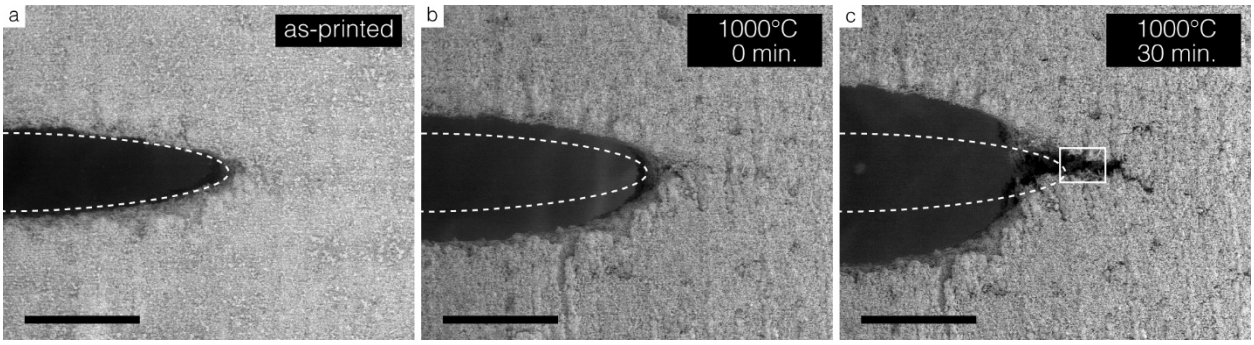

Fig. 4. Time-series SEM micrographs showing a sinter-cracking specimen at interrupted heating intervals: (a) the specimen as printed; (b) after being raised to 1000 °C and allowed to cool; (c) after sintering for 30 min at 1000 °C. The white dashed line indicates the original shape of the notch. Scale bars are 1 mm.

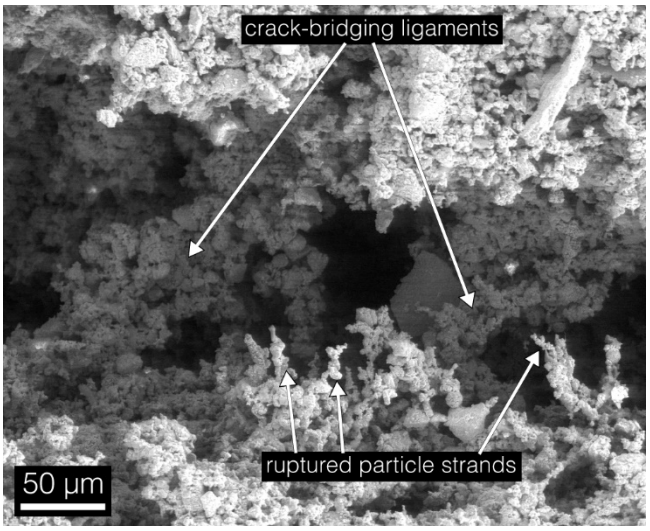

Fig. 5. Magnified view of the boxed area in Fig. 4c. Crack-bridging ligaments as well as ruptured particle strands are easily visible.

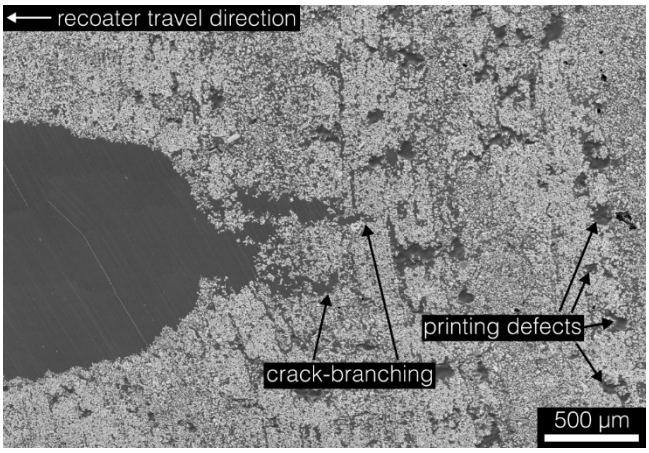

Fig. 6. Polished cross section of the specimen shown in Fig. 4c. Variations in porosity due to constrained sintering and the notch are evident, as well as defects from the 3D printing process. The crack which initiated from the notch root has branched as shown by the arrows. The direction of powder spreading is horizontal with respect to the figure (indicated), the direction of binder application (via the printhead) is vertical, and the build direction is normal to the page.

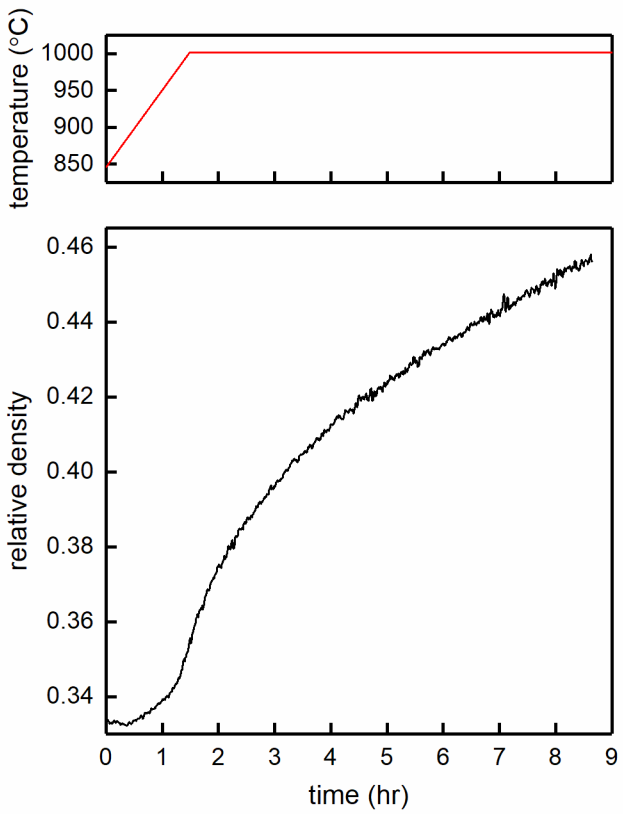

Fig. 7. Relative density as a function of time, measured from the *in situ* images by means of the projected specimen area and Eq. (1). Density measurements begin at a temperature of 845 °C. The sintering temperature of 1000 °C is reached at 1.5 hr and cracking begins at 1.4 hr. Data are shown until the point of complete fracture of the right side of the specimen.

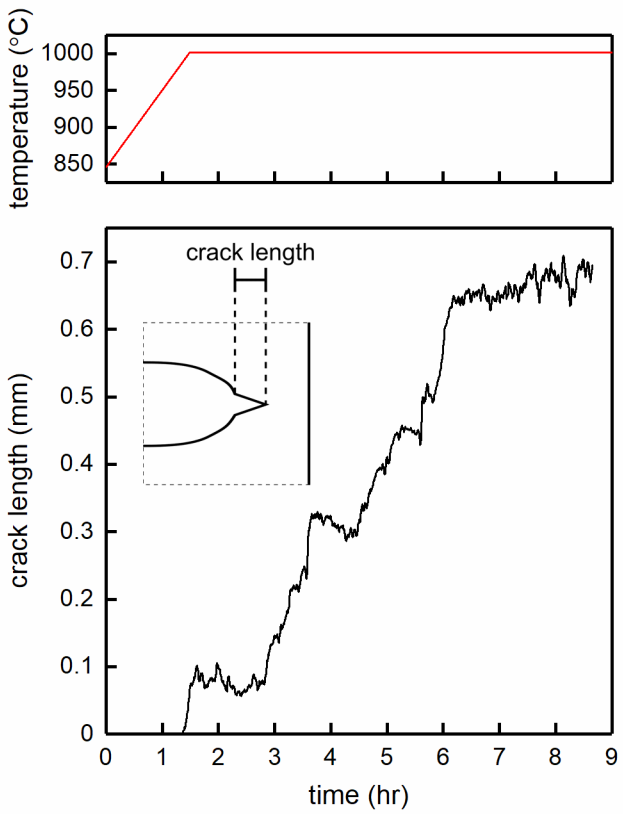

Fig. 8. Crack length as a function of time measured from the *in situ* images, spanning the same time as Fig. 7, with the temperature profile shown above. Crack length is determined with reference to the original notch root, as shown by the inset. Measurements are for the crack growing from the right side of the notch only. The sintering temperature of 1000 °C is reached at 1.5 hr, the second crack begins at 5.8 hr, and the terminus of the data represents complete fracture of the ligament.

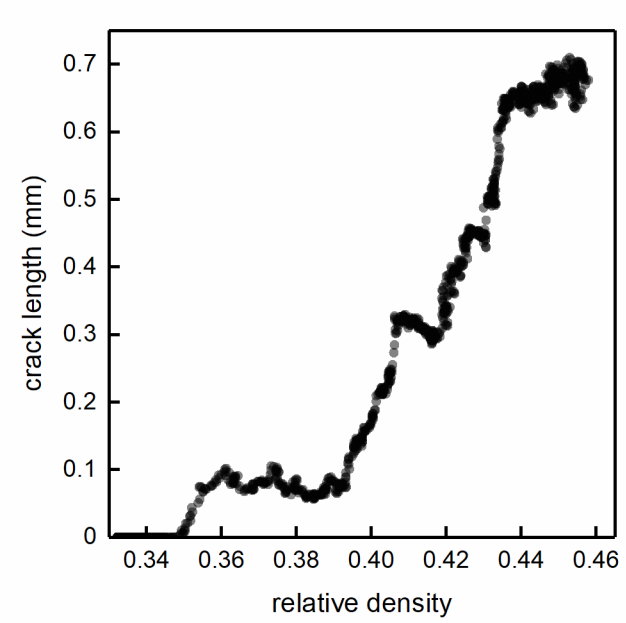

Fig. 9. Crack length plotted against the relative density as measured from the *in situ* images. An incubation phase of no cracking appears at low relative densities. Regions of growth and arrest are pronounced and show similar rates of change. The termination of the data represents total fracture of the right side of the specimen.